


The properties of supermassive black holes and their host galaxies for type 1 and 2 active galactic nuclei in the eFEDS and COSMOS fields

G. Mountrichas¹  and I. Georgantopoulos²

¹ Instituto de Física de Cantabria (CSIC-Universidad de Cantabria), Avenida de los Castros, 39005 Santander, Spain
e-mail: gmountrichas@gmail.com

² National Observatory of Athens, Institute for Astronomy, Astrophysics, Space Applications and Remote Sensing,
Ioannou Metaxa and Vasileos Pavlou, 15236 Athens, Greece

Received 4 October 2023 / Accepted 18 December 2023

ABSTRACT

In this study, our primary objective is to compare the properties of supermassive black holes (SMBHs) and their host galaxies between type 1 and type 2 active galactic nuclei (AGNs). In our analysis, we use X-ray detected sources in two fields, namely the eFEDS and the COSMOS-Legacy. To classify the X-ray sources, we performed a spectral energy distribution (SED) fitting analysis, using the CIGALE code. The robustness of our analysis was paramount so, to ensure this, we imposed stringent selection criteria. Thus, only sources with extensive photometric data across the optical, near- and mid-infrared part of the spectrum and reliable host galaxy properties and classifications were included. The final sample consists of 3312 AGNs, of which 3049 are classified as type 1 and 263 as type 2. The sources span a redshift range of $0.5 < z < 3.5$ and encompass a wide range of X-ray luminosities, falling within $42 < \log_{10} [L_{X,2-10\text{keV}} (\text{erg s}^{-1})] < 46$. Our results show that type 2 AGNs exhibit a tendency to inhabit more massive galaxies, by 0.2–0.3 dex (on a logarithmic scale), compared to type 1 sources. Type 2 AGNs also display, on average, lower specific black hole accretion rates, a proxy of the Eddington ratio, compared to type 1 AGNs. These differences persist across all redshifts and L_X considered within our dataset. Moreover, our analysis uncovers that type 2 sources tend to have lower star formation rates compared to type 1 AGNs at $z < 1$. This picture reverses at $z > 2$ and $\log_{10} [L_{X,2-10\text{keV}} (\text{erg s}^{-1})] > 44$. Similar patterns emerge when we categorize AGNs based on their X-ray obscuration levels (N_{H}). However, in this case, the observed differences are pronounced only for low-to-intermediate L_X AGNs and are also sensitive to the N_{H} threshold applied for the AGN classification. These comprehensive findings enhance our understanding of the intricate relationships governing AGN types and their host galaxy properties across diverse cosmic epochs and luminosity regimes.

Key words. Galaxy: evolution – galaxies: active – galaxies: formation – galaxies: nuclei – galaxies: statistics – X-rays: galaxies

1. Introduction

Active galactic nuclei (AGNs) occupy a pivotal role in the process of galaxy evolution. These AGNs derive their energy from the accretion of matter onto the supermassive black hole (SMBH) situated at the heart of galaxies. The co-evolution of AGNs and their host galaxies is intricately regulated by mechanisms governing SMBH accretion and subsequent feedback from AGNs. In order to unravel this complex interaction between the active SMBH and its host galaxy, it becomes imperative to gain insights into the internal structure of AGNs. A fundamental aspect of this endeavor involves elucidating the physical distinctions that underlie obscured and unobscured AGNs.

According to the unification model (e.g., Urry & Padovani 1995; Nenkova et al. 2002; Netzer 2015), an AGN is classified as obscured or unobscured based on the angle of our line of sight relative to the symmetry axis of the accretion disk and torus surrounding the central black hole. When we observe the AGN edge-on, we classify it as obscured, whereas an AGN is unobscured when it is viewed face-on. As the understanding of AGN structures has evolved, more intricate models (Ogawa et al. 2021; Esparza-Arredondo et al. 2021) have emerged to accommodate diverse classifications observed across various wave-

lengths. These models aim to account for the variety of classifications across different wavelengths (for instance, distinctions between X-ray and optical classifications; Ordovas-Pascual et al. 2017). However, despite these advancements, the primary determinant for discerning obscured and unobscured AGN, according to the unification model, continues to be the inclination angle.

An alternative interpretation of AGN obscuration arises within the realm of evolutionary models. According to this perspective, the distinct AGN types are attributed to the fact that SMBHs and their host galaxies are observed during different evolutionary phases. The core concept underlying these models posits that obscured AGNs are observed during an early phase when the energy output generated by the accretion disk surrounding the SMBH is not sufficiently robust to disperse the surrounding gas. As material continues to accrete onto the SMBH, its energy output intensifies, eventually compelling the obscuring material to dissipate (e.g., Ciotti & Ostriker 1997; Hopkins et al. 2006).

Obtaining a deeper understanding of the characteristics of both AGN populations is crucial to unveiling various facets of the intricate relationship between AGNs and galaxies. One commonly adopted method to accomplish this is to compare the host galaxy properties of obscured and unobscured AGNs. If the two

populations live in similar environments, this would provide support to the unification model, whereas if they reside in galaxies of different properties, it would suggest that they are observed at different evolutionary phases.

Active galactic nuclei can be classified into obscured and unobscured through diverse criteria. For example, the classification into these two groups can be accomplished using X-ray criteria, such as relying on the hydrogen column density or the hardness ratio (Mountrichas et al. 2020). Furthermore, optical spectral features contribute to the classification of AGNs into type 1 (unobscured) and type 2 (obscured). Type 1 AGNs exhibit broad lines in their optical spectra, while type 2 AGNs lack these broad emission lines (Zou et al. 2019). Notably, intermediate optical spectroscopic classifications, such as sub-types 1.0, 1.2, 1.5, 1.8, and 1.9, are also viable within this framework (Whittle 1992). Another classification method involves categorizing AGNs into type 1 and type 2 based on their inclination angle, i , determined through spectral energy distribution (SED) fitting (Mountrichas et al. 2022a). In this case, the subcategorization of AGNs is not possible since the calculation of i through SED fitting analysis is not sensitive to incremental changes in i (e.g., Yang et al. 2020). It is well acknowledged that the classification of AGNs may vary when employing these distinct criteria (e.g. Masoura et al. 2020; Mountrichas et al. 2022a).

Prior investigations that relied on optical criteria, such as optical spectra, to classify X-ray AGNs into type 1 and 2 found that type 2 sources tend to inhabit more massive systems compared to type 1, but no statistically significant differences were found regarding the star formation rate (SFR) of the two AGN populations. It is important to note, though, that these earlier studies concentrated on AGNs primarily within the realm of low-to-moderate X-ray luminosities, $\log [L_{X,2-10\text{keV}}(\text{erg s}^{-1})] < 44$ AGNs (Zou et al. 2019), and/or they restricted their analysis to low redshifts ($z < 1$; Mountrichas et al. 2021a).

Alternatively, AGNs are classified into obscured and unobscured using X-ray criteria. For instance, using the hydrogen column density, N_{H} , and a threshold at $N_{\text{H}} = 10^{21.5} \text{ cm}^{-2}$ (or $N_{\text{H}} = 10^{22} \text{ cm}^{-2}$), previous studies found no significant differences regarding the SFR and stellar mass, M_* , of galaxies hosting X-ray absorbed and unabsorbed AGNs (e.g., Masoura et al. 2021; Mountrichas et al. 2021c). More recently, Georgantopoulos et al. (2023) has adopted a higher N_{H} threshold ($N_{\text{H}} = 10^{23} \text{ cm}^{-2}$) and finds that the two AGN populations live in galaxies with statistically significant differences ($>2\sigma$) in terms of their SFR and M_* . Moreover, X-ray absorbed sources tend to exhibit lower specific black hole accretion rates, λ_{SMBHAR} , which serves as a proxy for the Eddington ratio, compared to their unabsorbed counterparts. They attribute these divergent findings compared to previous investigations to either the elevated N_{H} threshold employed or the varying X-ray luminosities probed by the datasets used across different studies. Mountrichas et al. (2024) have built upon these insights by employing X-ray AGN data from the 4XMM catalog and implementing rigorous X-ray criteria for AGN classification. Their results closely mirror those obtained by Georgantopoulos et al. (2023), reinforcing the observed differences in host galaxy properties between X-ray obscured and unobscured AGNs. Moreover, their analysis highlights that these distinctions tend to diminish for luminous AGNs. However, it's worth noting that the application of X-ray and optical criteria to AGN categorization may not always yield identical classifications (e.g., Masoura et al. 2020; Mountrichas et al. 2020).

In this work, we use X-ray AGNs detected in the eROSITA Final Equatorial Depth Survey (eFEDS) and the COSMOS-Legacy fields. Our primary objective revolves around comparing

the SMBH and host galaxy properties of type 1 and 2 AGNs. Sources were classified using the outcomes from applying an SED fitting analysis, employing the CIGALE code. Specifically, the measurement of the inclination angle, provided by CIGALE, was used for the AGN categorization. Section 3 presents the SED fitting analysis, the photometric data, and the quality selection criteria applied. These criteria were designed to identify sources with robust host galaxy measurements and reliable classifications. Additionally, the section elaborates on the criteria utilized to differentiate AGNs into the two distinct types. The presentation and discussion of our findings are provided in Sects. 4 and 5, respectively. We summarize our main conclusions in Sect. 6.

2. Data

In our analysis, we use X-ray AGNs detected in the eFEDS and COSMOS fields. Both datasets and the quality criteria applied are described in detail in Sect. 2 of Mountrichas et al. (2022a) and Mountrichas et al. (2022b). Below, we present a brief summary.

2.1. X-ray sources in the eFEDS field

The eFEDS X-ray catalog includes 27910 X-ray sources detected in the 0.2–2.3 keV energy band with detection likelihoods ≥ 6 , which corresponds to a flux limit of $\approx 7 \times 10^{-15} \text{ erg cm}^{-2} \text{ s}^{-1}$ in the 0.5–2.0 keV energy range (Brunner et al. 2022). Salvato et al. (2022) present the multi-wavelength counterparts and redshifts of the X-ray sources by identifying their optical counterparts. Two independent methods were utilized to find the counterparts of the X-ray sources, NWAY (Salvato et al. 2018) and ASTROMATCH (Ruiz et al. 2018). NWAY is based on Bayesian statistics and ASTROMATCH on the maximum likelihood ratio (Sutherland & Saunders 1992). For 88.4% of the eFEDS point-like sources, the two methods point at the same counterpart. Each counterpart was assigned a quality flag, CTP_QUALITY. Counterparts with CTP_QUALITY ≥ 2 were considered reliable, in the sense that either both methods agreed on the counterpart and had assigned a counterpart probability above the threshold (CTP_QUALITY = 4 for 20873 sources), or both methods agreed on the counterpart but one method had assigned a probability above the threshold (CTP_QUALITY = 3, 1379 sources), or there was more than one possible counterpart (CTP_QUALITY = 2, 2522 sources). Only sources with CTP_QUALITY ≥ 3 are included in our analysis. Moreover, Mountrichas et al. (2022a) crossmatched the X-ray dataset with the GAMA-09 photometric catalog produced by the HELP collaboration (Shirley et al. 2019, 2021), which covers $\sim 35\%$ of the eFEDS area, to extend the photometric coverage to far-infrared wavelengths. HELP provides data from 23 extragalactic fields imaged by the *Herschel* Space Observatory, which form the *Herschel* Extragalactic Legacy Project (HELP). About $\sim 10\%$ of the X-ray sources in the eFEDS field have available *Herschel*/SPIRE photometry.

eFEDS has been observed by a number of spectroscopic surveys, such as GAMA (Baldry et al. 2018), SDSS (Blanton et al. 2017), and WiggleZ (Drinkwater et al. 2018). Only sources with a secure spectroscopic redshift, *specz*, from the parent catalogs were considered in the eFEDS catalog (Salvato et al. 2022). 6640 sources have reliable *specz*. Photometric redshifts, *photoz*, were computed for the remaining sources using the LePHARE code (Arnouts et al. 1999; Ilbert 2006) and following the procedure outlined in, for example, Salvato et al. (2009, 2011). A redshift flag was assigned to each source, CTP_REDSHIFT_GRADE. Only sources with

CTP_REDSHIFT_GRADE ≥ 3 (26047/27910) are considered in this work. This criterion includes sources with either a spectroscopic redshift (CTP_REDSHIFT_GRADE = 5) or where the *photoz* estimates of the two methods agree (CTP_REDSHIFT_GRADE = 4) or agree within a tolerance level (CTP_REDSHIFT_GRADE = 3; for more details see Sect. 6.3 of Salvato et al. 2022).

Liu et al. (2022) performed a systematic X-ray spectral fitting analysis on all the X-ray systems. Based on their results, only 10% of the sources are X-ray obscured. In this work, we use their posterior median, intrinsic (absorption-corrected) X-ray fluxes in the 2–10 keV energy band.

2.2. X-ray sources in the COSMOS field

To increase the size of the sample used in our analysis, and in particular the number of type 2 AGNs, we also added sources detected in the COSMOS-Legacy survey (Civano et al. 2016). COSMOS-Legacy is a 4.6 Ms *Chandra* program that covers 2.2 deg² of the COSMOS field (Scoville et al. 2007). The central area has been observed with an exposure time of ≈ 160 ks, while the remaining area has an exposure time of ≈ 80 ks. The limiting depths are 2.2×10^{-16} , 1.5×10^{-15} and 8.9×10^{-16} erg cm⁻² s⁻¹ in the soft (0.5–2 keV), hard (2–10 keV), and full (0.5–10 keV) bands, respectively. The X-ray catalog includes 4016 sources. We only use sources within both the COSMOS and UltraVISTA (McCracken et al. 2012) regions. UltraVISTA covers 1.38 deg² of the COSMOS field (Laigle et al. 2016) and has deep near-infrared (NIR) observations (*J*, *H*, *K_s* photometric bands) that allow us to derive more accurate host galaxy properties through SED fitting (see below). There are 1718 X-ray sources that lie within the UltraVISTA area of COSMOS.

Marchesi et al. (2016) matched the X-ray sources with optical and infrared counterparts using the likelihood ratio technique (Sutherland & Saunders 1992). Of the sources, 97% have an optical and IR counterpart and a *photoz* and $\approx 54\%$ have *specz*. *photoz* available in their catalog were produced following the procedure described in Salvato et al. (2011). The accuracy of photometric redshifts is found at $\sigma_{\Delta z/(1+z_{spec})} = 0.03$. The fraction of outliers ($\Delta z/(1+z_{spec}) > 0.15$) is $\approx 8\%$. Mountrichas et al. (2022b) cross-matched the X-ray catalog with the COSMOS photometric dataset produced by the HELP collaboration to assign far-infrared photometry to the sources. About $\sim 60\%$ of the X-ray sources in the UltraVISTA region have available *Herschel*/SPIRE photometry.

The catalog presented in Marchesi et al. (2016) also provides measurements of the intrinsic column density, N_H , estimated using hardness ratios ($HR = \frac{H-S}{H+S}$, where H and S are the net counts of the sources in the hard and soft bands, respectively) and the method (Bayesian estimation of hardness ratios, BEHR) presented in Park et al. (2006). An X-ray spectral power law with slope $\Gamma = 1.8$ was also assumed.

3. Analysis

In this section, we outline the methodology employed to measure the host galaxy properties of the X-ray sources and describe the criteria utilized for the selection of sources with the most robust measurements and reliable classification.

3.1. Host galaxy properties

The host galaxy properties of the X-ray AGNs have been calculated via SED fitting, using the CIGALE code (Boquien et al.

2019; Yang et al. 2020, 2022). The SED fitting analysis is described in detail in Sect. 3.1 in Mountrichas et al. (2022b) and Mountrichas et al. (2022a) for sources in the COSMOS and eFEDS fields, respectively.

In brief, the galaxy component is modeled using a delayed SFH model with a function form $SFR \propto t \times \exp(-t/\tau)$. A star formation burst is included (Małek et al. 2018; Buat et al. 2019) as a constant ongoing period of star formation of 50 Myr. Stellar emission is modeled using the single stellar population templates of Bruzual & Charlot (2003) and is attenuated following the Charlot & Fall (2000) attenuation law. To model the nebular emission, CIGALE adopts the nebular templates based on Villa-Velez et al. (2021). The emission of the dust heated by stars is modeled based on Dale et al. (2014), without any AGN contribution. The AGN emission is included using the SKIRTOR models of Stalevski et al. (2012, 2016). The parameter space used in the SED fitting process is shown in Table 1 in Mountrichas et al. (2022a,b). CIGALE has the ability to model the X-ray emission of galaxies. In the SED fitting process, the intrinsic L_X in the 2–10 keV band, provided in the Marchesi et al. (2016) for the COSMOS dataset and in Liu et al. (2022) for the eFEDS sample, are used. The reliability of the SFR measurements has been examined in detail in our previous works and, in particular, in Sect. 3.2.2 in Mountrichas et al. (2022b).

3.2. Selection of AGN with robust SED fitting measurements

In order to get reliable SED fitting results, it is essential to restrict the analysis to those sources with the highest possible photometric coverage. For that purpose, Mountrichas et al. (2022b,a) required the X-ray AGNs to have available the following photometric bands: *u*, *g*, *r*, *i*, *z*, *J*, *H*, *K*, *W1*/IRAC1, *W2*/IRAC2, and *W4*/MIPS24, where *W1*, *W2*, and *W4* are the photometric bands of WISE (Wright et al. 2010), at 3.4 μ m, 4.6 μ m, and 22 μ m, respectively, and IRAC1, IRAC2, and MIPS24 are the 3.6 μ m, 4.5 μ m, and 24 μ m photometric bands of *Spitzer*. They also applied the following requirements in CIGALE's results: a reduced χ^2 threshold of $\chi_r^2 < 5$ was imposed (e.g. Masoura et al. 2018; Buat et al. 2021) and sources for which CIGALE could not constrain the parameters of interest (SFR, M_*) were excluded from the analysis. Specifically, CIGALE provides two values for each estimated galaxy property. One value corresponds to the best model and the other value (bayes) is the likelihood-weighted mean value. A large difference between the two calculations suggests a complex likelihood distribution and important uncertainties. Therefore, in our analysis we included only sources for which $\frac{1}{5} \leq \frac{SFR_{best}}{SFR_{bayes}} \leq 5$ and $\frac{1}{5} \leq \frac{M_{*,best}}{M_{*,bayes}} \leq 5$, where SFR_{best} and $M_{*,best}$ are the best-fit values of SFR and M_* , respectively, and SFR_{bayes} and $M_{*,bayes}$ are the Bayesian values estimated by CIGALE.

In the SED fitting analysis followed by Mountrichas et al. (2022a), they used the Gaussian aperture and photometry (GAAP) photometry that is available in the eFEDS X-ray catalog. GAAP photometry was performed twice, with the aperture setting MIN_APER = 0'7 and 1'0. A value is provided for each photometric band with the optimal MIN_APER (for the choice of GAAP aperture size, see Kuijken et al. 2015). GAAP was optimized to calculate *photoz* that require colour measurements. In the case of extended and low redshift sources, total fluxes may be underestimated (Kuijken et al. 2019). Due to these considerations, they opted to omit sources with low redshift values ($z < 0.5$) from their analysis. We adhered to their rationale and also implemented the identical redshift limit in our analysis.

For consistency, the same requirement was applied to the X-ray AGNs in the COSMOS field.

The application of the criteria above and those mentioned in Sect. 2 results in 7279 AGNs. Out of them, 2727 (37%) have a spectroscopic redshift. Of the 7279, 6131 (84%) were detected in the eFEDs field and 1148 in the UltraVISTA region of COSMOS.

3.3. Classification of AGNs

Mountrichas et al. (2021a) used X-ray AGNs in the XMM-XXL field (Pierre et al. 2016) and show that CIGALE can reliably classify sources into type 1 and 2. Specifically, they identify type 1 and 2 AGNs, using the bayes and best estimates of the i parameter, derived by CIGALE. Type 1 AGNs, based on the SED analysis, are those with $i_{\text{best}} = 30^\circ$ and $i_{\text{bayes}} < 40^\circ$, while secure type 2 sources are those with $i_{\text{best}} = 70^\circ$ and $i_{\text{bayes}} > 60^\circ$. Then, they compare CIGALE’s classification with that provided in the catalog presented in Menzel (2016), in which AGNs are divided into broad (type 1) and narrow (type 2) line sources, using the full width half maximum (FWHM) for emission lines originating in different regions of the AGNs (H_β , MgII, CIII, and CIV).

The analysis presented in Mountrichas et al. (2021a) reveals that the SED fitting algorithm classifies type 1 AGNs with an accuracy of $\sim 85\%$. A similar percentage is found regarding the completeness at which type 1 sources are identified. For type 2 sources, the performance of CIGALE is at $\sim 50\%$, both regarding the reliability and the completeness. We note that the reliability is defined as the fraction of the number of type 1 (or type 2) sources classified by the SED fitting that are similarly classified by optical spectra. The completeness refers to how many sources classified as type 1 (or type 2) based on optical spectroscopy were identified as such by the SED fitting results. Therefore, for the purposes of this work, we are mainly interested in the reliability performance of CIGALE.

The reliability of $\sim 85\%$ with which CIGALE identifies type 1 sources is acceptable for the purposes of our statistical analysis. However, the reliability of the SED fitting code regarding type 2 AGNs is rather low, since it implies that about half of the sources identified as type 2 by CIGALE are, in fact, misclassified sources. Nevertheless, Mountrichas et al. (2021a) show that the vast majority ($\sim 82\%$) of the misclassified type 2 sources have increased polar dust values ($E_{B-V} > 0.15$; see their Fig. 8 and Sect. 5.1.1). Thus, we excluded these sources from our analysis and classified as type 2 those AGNs that meet the inclination angle criteria mentioned above and also have polar dust values lower than $E_{B-V} < 0.15$. We note, that the introduction of polar dust in the fitting process improves the accuracy of CIGALE in the source type classification, in particular in its reliability to identify type 2 sources (see Sect. 5.5 in Mountrichas et al. 2021b).

Moreover, it is essential to emphasize that not all of the excluded type 2 sources would be categorized as type 1 based on optical spectra. For example, in the study by Mountrichas et al. (2021a), a substantial proportion of sources that CIGALE identified as type 2 and that exhibited elevated polar dust content were subsequently confirmed as type 2 through spectroscopic classification ($\frac{9}{32} = 28\%$). However, as was previously mentioned, the exclusion of these systems enhances the reliability of CIGALE in discerning type 2 AGNs, as is supported by the findings in Mountrichas et al. (2021a).

The application of these criteria to the 7249 AGNs (see previous section) results in 3312 reliably classified sources (Table 1).

Table 1. Number of type 1 and 2 AGNs.

Field	Type 1	Type 2
eFEDS	2696	147
COSMOS	353	116
Total	3049	263

Notes. Sources are classified by CIGALE, based on the inclination angle measurements (see text for more details).

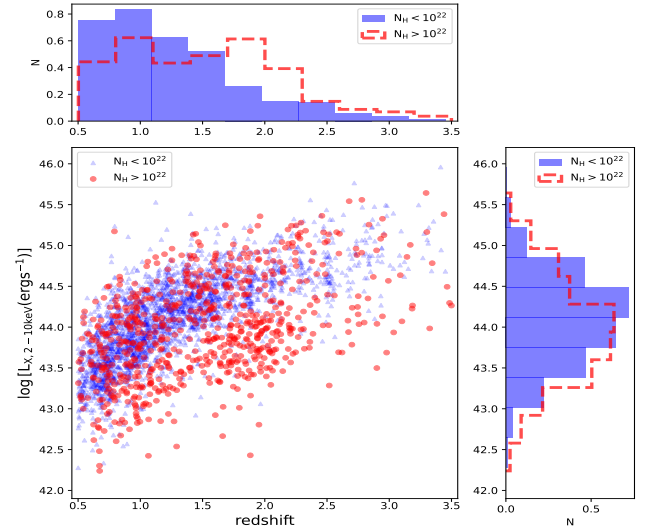


Fig. 1. Distribution of type 1 (blue triangles) and type 2 (red circles) AGNs used in our analysis, in the L_X -redshift plane.

3049 of them are type 1 (2696 in eFEDS and 353 in COSMOS) and 263 are type 2 (147 in eFEDS and 116 in COSMOS). Their distribution in the L_X -redshift plane is shown in Fig. 1. These are the sources that we used in our analysis.

4. Results

In this section, we perform a comparative analysis of the SFR and M_* between galaxies hosting type 1 and 2 AGNs. Additionally, we explore potential distinctions in the λ_{sBHAR} for these two AGN populations.

For that purpose, we split the X-ray AGN dataset into three redshift intervals, that is, $0.5 < z < 1.0$, $1.0 < z < 2.0$, and $2.0 < z < 3.5$, and compared the distributions of SFR, M_* , and λ_{sBHAR} of type 1 and 2 AGNs. In all cases, the distributions were weighted to account for the different redshift and L_X of the two AGN populations, following the process described in, for instance, Mountrichas et al. (2019, 2021a), Masoura et al. (2021), Buat et al. (2021), Koutoulidis et al. (2022). Specifically, a weight was assigned to each source. This weight was calculated by measuring the joint L_X distributions of the two populations (i.e., we added the number of type 1 and 2 AGNs in each L_X bin, in bins of 0.1 dex) and then normalizing the L_X distributions by the total number of sources in each bin. The same procedure was followed for the redshift distributions of the two AGN populations. The total weight that was assigned in each source was the product of the two weights. We made use of these weights in all the distributions presented in the remainder of this section.

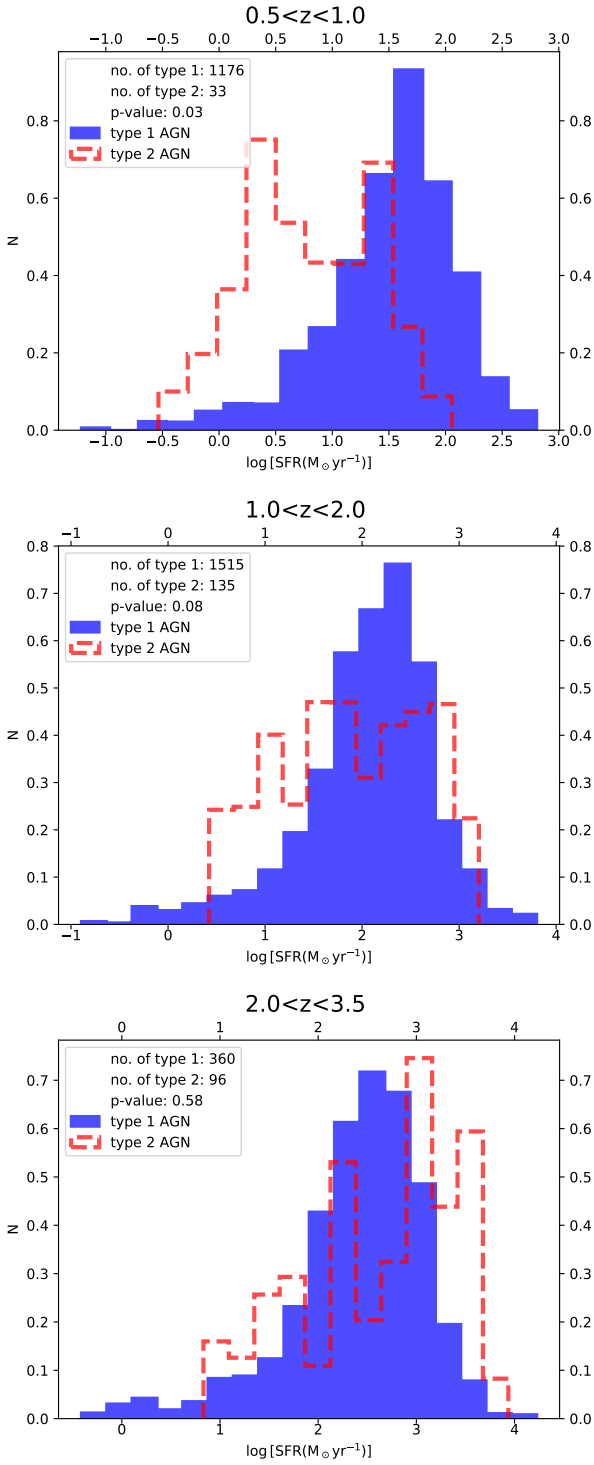


Fig. 2. Distributions of SFRs of type 1 (blue shaded histogram) and type 2 (red, dashed histogram) at different redshift intervals, as is indicated in the title of each panel. The distributions were weighted to account for the different L_X and redshift of the two AGN populations (see text for more details).

4.1. Star formation rates of type 1 and 2 AGNs

First, we compare the SFRs of the two AGN types. The results are shown in Fig. 2, for the three redshift intervals. We notice that, with the exception of the highest redshift interval, type 2 sources tend to have lower SFRs compared to their type 1 counterparts. The Kolmogorov-Smirnov (KS) test reveals that this

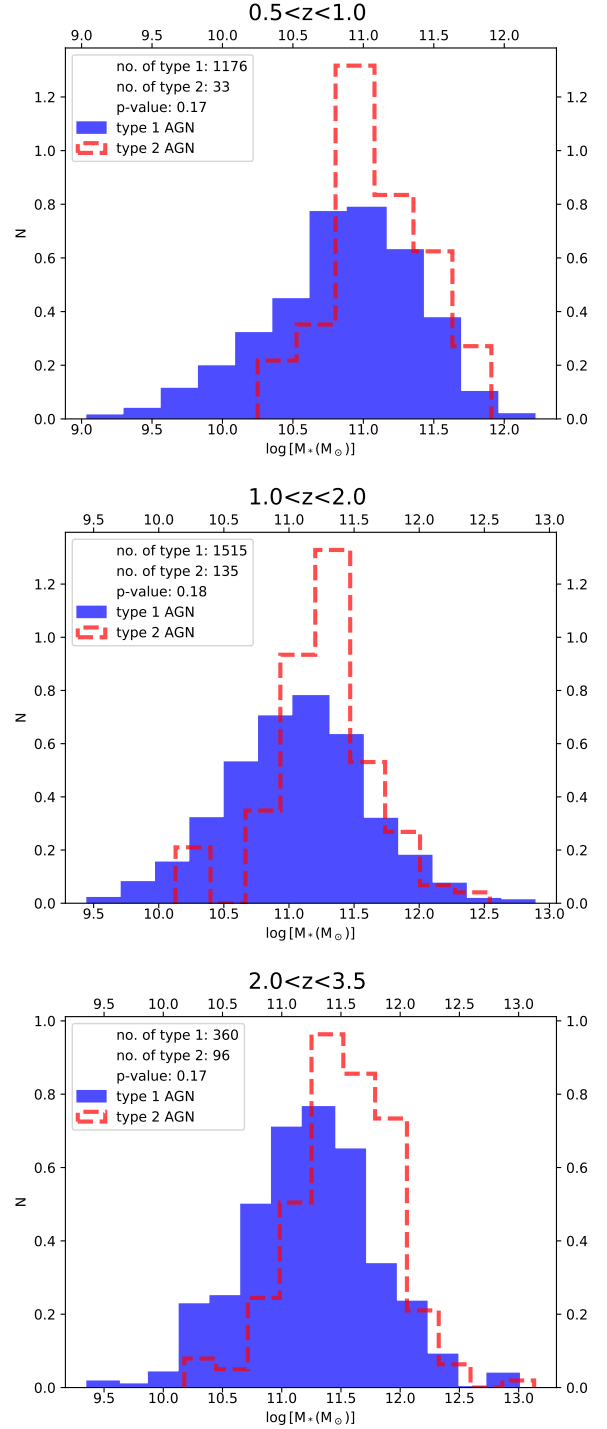


Fig. 3. Distributions of M_* of type 1 (shaded blue histogram) and type 2 (dashed red histogram) at different redshift intervals, as is indicated in the title of each panel. The distributions were weighted to account for the different L_X and redshift of the two AGN populations (see text for more details).

discrepancy has a statistical significance beyond the level of 2σ at the lowest redshift bin (p value of 0.03). In statistical terms, two distributions are considered to differ with a significance of approximately 2σ for a p value of 0.05, a threshold commonly employed in similar studies to assess the statistical significance of differences between distributions (e.g., Zou et al. 2019; Mountrichas et al. 2021a; Georgantopoulos et al. 2023).

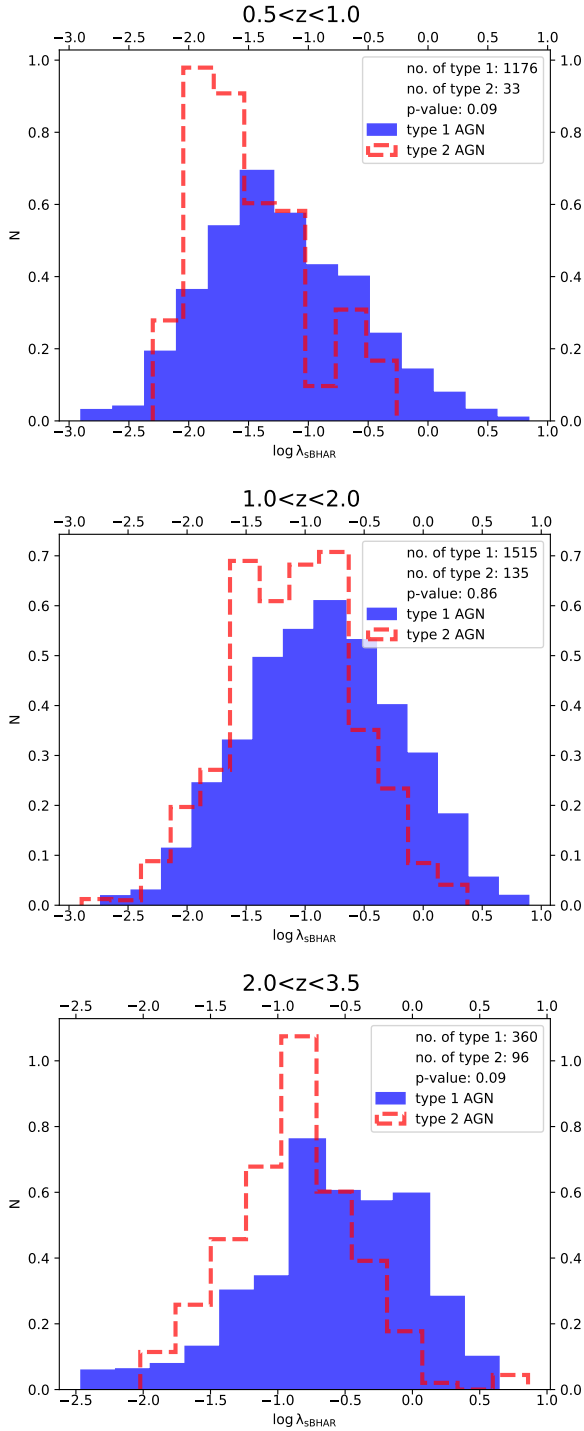


Fig. 4. Distributions of λ_{sBHAR} of type 1 (shaded blue histogram) and type 2 (dashed red histogram) at different redshift intervals, as is indicated in the title of each panel. The distributions were weighted to account for the different L_X and redshift of the two AGN populations (see text for more details).

The two AGN populations appear to have similar SFRs at the highest redshift range probed by the dataset used in our analysis. The (weighted) median SFR values for the two AGN types are presented in Table 2.

It is worth noting that these trends persist even when we restrict our X-ray dataset to sources with *specz*, resulting in a subset of 1308 type 1 AGNs and 150 type 2 AGNs within the

redshift range of $0.5 < z < 3.5$. Additionally, these overarching conclusions hold when we consider the two fields separately, though the difference between the two AGN types is less pronounced in SFRs at $0.5 < z < 1.0$. Finally, we note that the SFR difference is not affected if we restrict type 1 sources to only those with low levels of polar dust ($E_{B-V} < 0.15$, i.e., similarly to type 2 AGNs).

4.2. Stellar mass of type 1 and 2 AGNs

A comparison of the M_* distributions of the two AGN populations, shown in the three panels of Fig. 3, reveals that type 2 sources tend to live in more massive systems compared to type 1 ones, by 0.15–0.30 dex. The (weighted) median M_* values for the two AGN types are presented in Table 2. This difference, although it is only statistically significant at a level lower than 2σ , appears to be consistent across all the redshifts spanned by our sample. We also confirm that the results remain unchanged if we restrict the analysis to sources with *specz* and if we examine the two fields separately.

4.3. Specific black hole accretion rate of type 1 and 2 AGNs

Finally, we compare the λ_{sBHAR} distributions of type 1 and 2 AGNs. λ_{sBHAR} is defined as

$$\lambda_{\text{sBHAR}} = \frac{k_{\text{bol}} L_{X,2-10\text{keV}}}{1.26 \times 10^{38} \text{ erg s}^{-1} \times 0.002 \frac{M_*}{M_\odot}}, \quad (1)$$

where k_{bol} is a bolometric correction factor that converts the 2–10 keV X-ray luminosity into an AGN bolometric luminosity. We adopted a value of 25 for k_{bol} in line with previous studies (e.g., Elvis et al. 1994; Georgakakis et al. 2017; Aird et al. 2018; Mountrichas et al. 2021c, 2022b), although it is worth noting that lower values (e.g., $k_{\text{bol}} = 22.4$ in Yang et al. 2017) and luminosity-dependent bolometric corrections (e.g., Hopkins et al. 2007; Lusso 2012) have also been employed in the literature.

Although, λ_{sBHAR} is often used as a proxy of the Eddington ratio, it is important to acknowledge that the calculation of the AGN bolometric luminosity and the inherent scatter in the relation between the black hole mass, M_{BH} , and M_* , may introduce variations in λ_{sBHAR} compared to the Eddington ratio, as has been indicated by previous studies (Lopez et al. 2023; Mountrichas & Buat 2023). Nevertheless, our primary objective is to explore potential disparities in the distributions of λ_{sBHAR} between type 1 and type 2 AGNs.

The λ_{sBHAR} distributions of the two AGN classes are presented in the three panels of Fig. 4 and the (weighted) median values in Table 2. Based on the results, type 1 AGNs appear to have higher λ_{sBHAR} values, by ~ 0.25 dex, in all the three redshift intervals used in our analysis. We confirm that the results are not sensitive to the accuracy of the calculated redshifts (total vs. *specz* only) and to cosmic variance.

4.4. The effect of L_X

Subsequently, we split the X-ray dataset into high and low-to-intermediate L_X sources, utilizing a cut at $\log [L_{X,2-10\text{keV}} (\text{erg s}^{-1})] > 44$. Our goal is to examine if the trends we observed are luminosity-dependent. Table 3 displays the weighted median values of SFR, M_* , and λ_{sBHAR} for both AGN types within the two L_X regimes. Additionally, the table includes the p values derived from conducting

Table 2. Number of sources, the corresponding values of SFR, M_* , and λ_{SBHAR} and p -values for type 1 and 2 sources, in the three redshift intervals used in our analysis.

	$0.5 < z < 1.0$		$1.0 < z < 2.0$		$2.0 < z < 3.5$	
	Type 1	Type 2	Type 1	Type 2	Type 1	Type 2
Number of sources	1178	33	1515	135	360	96
log SFR	1.60	0.76	2.16	1.86	2.51	2.87
p value (SFR)		0.03		0.08		0.58
log M_*	10.89	11.04	11.07	11.28	11.24	11.53
p value (M_*)		0.17		0.18		0.17
log λ_{SBHAR}	-1.29	-1.55	-0.86	-1.10	-0.55	-0.86
p value (λ_{SBHAR})		0.09		0.86		0.09

Notes. Weighted median values of SFR, M_* , and λ_{SBHAR} are presented. p -values are yielded by applying KS test.

the KS test to assess the distinctions among the different distributions.

In terms of M_* and λ_{SBHAR} , while the differences appear statistically significant at a level lower than 2σ , we observe a consistent pattern across all redshifts and luminosity ranges encompassed by our dataset. Specifically, both low-to-intermediate and high L_X type 2 AGNs exhibit a preference for more massive systems (albeit with a margin of only 0.1–0.2 dex) compared to their type 1 counterparts, along with lower values of λ_{SBHAR} . Therefore, we can conclude that the differences observed in these two parameters (M_* and λ_{SBHAR}) remain consistent across all redshifts up to 3.5 and are not contingent on AGN luminosity.

Concerning the SFRs of the two AGN populations, it appears that type 2 sources with $\log, [L_{X,2-10\text{keV}}(\text{erg s}^{-1})] < 44$ tend to have lower SFRs compared to type 1 AGNs. However, in the case of the most luminous AGN ($\log, [L_{X,2-10\text{keV}}(\text{erg s}^{-1})] > 44$), this pattern is only valid at redshifts below 1, and the situation reverses in the highest redshift interval ($z > 2$), where luminous type 2 AGNs tend to exhibit higher SFRs compared to luminous type 1 AGNs. Most of these differences appear statistically significant at a 2σ level.

Overall, we conclude that type 2 sources prefer to live in more massive host galaxies and tend to have lower λ_{SBHAR} compared to type 1 X-ray AGNs, at all redshifts and L_X spanned by our dataset. Moreover, low-to-moderate L_X type 2 systems appear to have lower SFRs compared to their type 1 counterparts. This picture reverses at high L_X ($\log, [L_{X,2-10\text{keV}}(\text{erg s}^{-1})] > 44$) and redshift $z > 2$. The fact that most of these differences are statistically significant at a level lower than 2σ can be attributed to the contamination in CIGALE’s classification. As has been noted, previous studies have shown that CIGALE misclassifies 10–20% of the sources.

4.5. Classification based on X-ray obscuration

To facilitate a more direct comparison with previous studies that relied on X-ray criteria to classify AGNs, we divided the 3312 sources with a reliable CIGALE classification (Table 1) into X-ray absorbed and unabsorbed ones, using a cut at $N_{\text{H}} = 10^{23} \text{ cm}^{-2}$, and repeated our analysis. There are 145 X-ray absorbed AGNs in our dataset and 3167 X-ray unabsorbed ones. The results are presented in Table 4. Similarly to the results obtained using the classification from CIGALE, absorbed AGNs tend to have a lower λ_{SBHAR} and live, on average, in more massive galaxies that exhibit lower SFRs (although the latter is now observed at all redshifts spanned by our sample) compared to

their unabsorbed counterparts. However, with the exception of the SFR at $z < 2$, none of the other differences appear to be statistically significant ($< 2\sigma$).

Since the same trends are found independently of the redshift, we then merged the three redshift bins and split the sources into low and high L_X , utilizing a threshold at $\log[L_{X,2-10\text{keV}}(\text{erg s}^{-1})] = 44$. The results are displayed in Table 5. Based on our findings, it is primarily the low-to-intermediate L_X AGNs that present differences in the host galaxy and SMBH properties of the two AGN populations. These differences also appear to be statistically significant at a level of $\approx 2\sigma$. We also note that the observed trends diminish when we lower the N_{H} threshold used to classify AGNs to 10^{22} cm^{-2} .

5. Discussion

In this section, we discuss how our results compare with the findings of prior studies. Additionally, we delve into the influence of varying the classification criteria on the reported outcomes.

5.1. Obscuration and M_*

Zou et al. (2019) divided X-ray sources in the COSMOS field into type 1 and 2, based on their optical spectra, morphologies, and variability. They find that type 2 sources are inclined to inhabit more massive systems compared to type 1 ones, by 0.1–0.2 dex, up to $z \approx 3.5$. Mountrichas et al. (2021a) examined X-ray detected AGNs in the XMM-XXL field, at a median $z \approx 0.5$, and classified AGNs into two types using the classification that is available in the XXL catalog (Menzel 2016) and that is based on optical spectra. Their results are similar to those reported by Zou et al. (2019). Our findings align with the results of these previous studies. Different M_* for the different AGN populations have also been reported by studies that used X-ray classification criteria (Lanzuisi 2017; Georgantopoulos et al. 2023, but see Masoura et al. 2021; Mountrichas et al. 2021a).

5.2. Obscuration and the SFR

Neither of the previously mentioned investigations (Zou et al. 2019; Mountrichas et al. 2021a) discerned a significant disparity in the SFR of host galaxies between the two AGN populations. Our analysis, however, suggests that the hosts of type 1 and 2 sources have different SFRs and that this difference represents a dependence on the redshift and L_X . It is worth noting that the sources utilized in Mountrichas et al. (2021a) primarily probe lower redshifts and span a narrower L_X range than

Table 3. Same as in Table 2, but now splitting the X-ray dataset into two L_X bins.

	$0.5 < z < 1.0$				$1.0 < z < 2.0$				$2.0 < z < 3.5$			
	$\log L_X < 44$		$\log L_X > 44$		$\log L_X < 44$		$\log L_X > 44$		$\log L_X < 44$		$\log L_X > 44$	
	Type 1	Type 2	Type 1	Type 2	Type 1	Type 2	Type 1	Type 2	Type 1	Type 2	Type 1	Type 2
Number of sources	918	25	258	8	412	49	1103	86	46	13	314	83
$\log \text{SFR}$	1.56	0.63	1.75	0.94	1.74	1.21	2.31	2.25	1.69	1.26	2.58	2.98
p value (SFR)	0.19		0.05		0.15		0.09		0.03		0.05	
$\log M_*$	10.90	10.95	10.88	11.04	11.05	11.28	11.07	11.29	11.20	11.31	11.25	11.58
p value (M_*)	0.42		0.13		0.52		0.29		0.12		0.43	
$\log \lambda_{\text{SBHAR}}$	-1.40	-1.58	-0.72	-0.86	-1.35	-1.58	-0.65	-0.89	-1.33	-1.52	-0.48	-0.81
p value (λ_{SBHAR})	0.62		0.64		0.29		0.52		0.22		0.11	

Table 4. Number of sources, the corresponding values of SFR, M_* , and λ_{SBHAR} and p -values for X-ray absorbed and unabsorbed sources, in the three redshift intervals used in our analysis.

	$0.5 < z < 1.0$		$1.0 < z < 2.0$		$2.0 < z < 3.5$	
	$<10^{23}$	$>10^{23}$	$<10^{23}$	$>10^{23}$	$<10^{23}$	$>10^{23}$
$\log [N_{\text{H}} (\text{cm}^{-2})]$						
Number of sources	1631	17	1130	80	406	48
$\log \text{SFR}$	1.65	0.07	2.20	1.33	2.44	1.89
p value (SFR)	0.03		0.03		0.31	
$\log M_*$	10.89	10.96	11.05	11.11	11.27	11.33
p value (M_*)	0.90		0.90		0.31	
$\log \lambda_{\text{SBHAR}}$	-1.27	-1.48	-0.89	-0.98	-0.76	-0.88
p value (λ_{SBHAR})	0.22		0.87		0.23	

Notes. Weighted median values of SFR, M_* , and λ_{SBHAR} are presented. Sources are classified using a threshold of $\log [N_{\text{H}} (\text{cm}^{-2})] = 23$. p -values are yielded by applying KS test.

Table 5. Same as in Table 4, but now splitting the X-ray dataset into two L_X bins.

	$0.5 < z < 3.5$			
	$\log L_X < 44$		$\log L_X > 44$	
	$<10^{23}$	$>10^{23}$	$<10^{23}$	$>10^{23}$
$\log [N_{\text{H}} (\text{cm}^{-2})]$				
Number of sources	1392	69	1775	76
$\log \text{SFR}$	1.69	1.06	2.39	1.49
p value (SFR)	0.02		0.36	
$\log M_*$	11.03	11.27	11.07	11.04
p value (M_*)	0.08		0.78	
$\log \lambda_{\text{SBHAR}}$	-1.38	-1.71	-0.66	-0.62
p value (λ_{SBHAR})	0.05		0.84	

our dataset, as is indicated in their Fig. 7. To facilitate a better comparison with Zou et al. (2019), we conducted a supplementary analysis by limiting our sample to sources within the COSMOS field. The outcomes of this restricted analysis indicate that the two AGN populations exhibit smaller differences in their SFR distributions up to a redshift of $z = 2$, and the statistical significance of these differences is notably low (p value ~ 0.60). In the highest redshift interval ($2.0 < z < 3.5$), the results obtained are similar to those using both datasets

The difference in the SFR has also been reported on in the literature by studies that classified X-ray AGNs using X-ray absorption criteria (Georgantopoulos et al. 2023, but see Lanzuisi 2017; Masoura et al. 2021; Mountrichas et al. 2021a).

Georgantopoulos et al. (2023) used AGNs in the COSMOS field and a high N_{H} threshold ($N_{\text{H}} = 10^{23} \text{ cm}^{-2}$) to classify X-ray sources into absorbed and unabsorbed ones. They observe that absorbed sources exhibit a tendency toward lower levels of the specific star formation rate (sSFR, defined as $\text{sSFR} = \frac{\text{SFR}}{M_*}$) when compared to unabsorbed sources. Georgantopoulos et al. attribute the disparities observed in their results, in contrast to prior research that found no discernible distinctions in the properties of host galaxies between X-ray absorbed and unabsorbed AGNs (e.g., Masoura et al. 2021; Mountrichas et al. 2021c), or research employing optical criteria (e.g., Zou et al. 2019; Mountrichas et al. 2021a), to variances in the N_{H} thresholds employed and/or the range of luminosities investigated

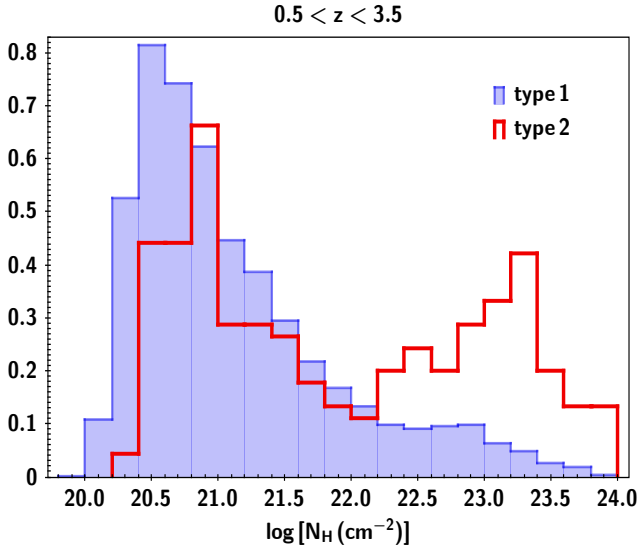


Fig. 5. Distribution of N_{H} , for type 1 (shaded blue histogram) and type 2 (dashed red histogram) AGNs.

by different sample sets. Mountrichas et al. (2024) used X-ray AGNs from the 4XMM dataset and applied strict X-ray criteria for the AGN classification ($N_{\text{H}} = 10^{23} \text{ cm}^{-2}$), taking into account also the uncertainties associated with the N_{H} measurements. Their findings closely mirror those reported in the study by Georgantopoulos et al. (2023) concerning the host galaxy properties of the two AGN populations. The aforementioned discrepancies were attributed to the varying ranges of L_{X} that different studies examined and not to the N_{H} threshold utilized for the AGN classification. Specifically, their analysis demonstrates that the observed distinctions in host galaxy properties between obscured and unobscured AGNs tend to diminish notably at higher levels of X-ray luminosity (specifically, when $\log[L_{\text{X},2-10 \text{ keV}} (\text{erg s}^{-1})] > 44$).

5.3. Obscuration and the Eddington ratio

Our study suggests that type 2 AGNs tend to have a lower λ_{SBHAR} compared to type 1 ones. Prior works that categorized AGNs based on optical criteria did not examine the difference in their n_{Edd} or λ_{SBHAR} . However, differences in n_{Edd} between the two populations have been reported by studies that used X-ray criteria to classify AGNs. These studies have shown that X-ray absorbed AGNs exhibit, on average, a lower n_{Edd} compared to their X-ray unabsorbed counterparts (Ricci et al. 2017; Ananna et al. 2022; Georgantopoulos et al. 2023), in agreement with our findings.

5.4. Concluding remarks

The picture that emerges is that when AGNs are classified as types 1 and 2 (e.g., using optical criteria), then type 2 AGNs appear to inhabit, on average, galaxies with a higher M_{*} than type 1 ones (this study, Zou et al. 2019; Mountrichas et al. 2021a). Type 2 sources are also hosted by systems exhibiting a lower SFR, but this difference is not universal and seems to hinge on redshift and, most importantly, on the L_{X} probed. Furthermore, type 2 AGNs also tend to have a lower λ_{SBHAR} (or n_{Edd}).

It is important to highlight that comparing results between studies that employ optical and X-ray criteria for AGN classifi-

cation can be challenging due to the considerable scatter in the correlation between optical obscuration and X-ray absorption. For instance, a source may be heavily X-ray obscured with broad UV-optical lines (e.g., Merloni et al. 2014; Li et al. 2019) and can be optically classified as type 2, without necessarily being X-ray absorbed (e.g., Masoura et al. 2020). Figure 5 presents the distribution of N_{H} for the type 1 and type 2 sources used in our analysis (at $0.5 < z < 3.5$). While type 2 AGNs typically exhibit higher N_{H} values than type 1 AGNs (median $\log [N_{\text{H}} (\text{cm}^{-2})] = 21.73$ and 20.90, for type 2 and type 1, respectively), it is crucial to acknowledge that these criteria would result in the classification of a significant number of sources in different ways. It is important to highlight that CIGALE lacks sensitivity to incremental changes in the inclination angle. Consequently, intermediate values of the estimated inclination angle should not be deemed reliable for categorizing AGNs into sub-classes. Therefore, certain sources identified as type 2 by CIGALE might actually be more akin to type 1.8 or 1.9, exhibiting similarities with type 1 rather than type 2 sources, as has been exemplified in studies such as Trippe et al. (2010), Hernández-García et al. (2017). These sources may also be characterized as X-ray unabsorbed, as is indicated by Shimizu et al. (2018). It is noteworthy, though, that these observations are not indicative of misclassification by CIGALE. Similar results are reported in Mountrichas et al. (2021a), where the categorization of AGNs into types 1 and 2 was based on optical spectra (see the right panel of their Fig. 7). Further investigation reveals that type 1 AGNs with $N_{\text{H}} > 10^{22} \text{ cm}^{-2}$ have a tendency for increased levels of polar dust, based on CIGALE measurements compared to type 1 AGNs with lower N_{H} . Specifically, the median E_{B-V} value for the former class is 0.22 and for the latter is 0.15. Mountrichas et al. (2021a) find that the majority of sources ($\sim 80\%$, i.e., $\frac{105}{105+27}$) classified as type 1 by CIGALE that also present elevated levels of polar dust ($E_{B-V} > 0.15$) are spectroscopically confirmed as type 1 (see their Fig. 8). Furthermore, there exists a significant fraction ($\sim 50\%$) of type 2 AGNs characterized by low levels of X-ray obscuration ($\log [N_{\text{H}} (\text{cm}^{-2})] < 22$). As was previously mentioned, such sources have been reported in the literature (e.g., Masoura et al. 2020). These findings collectively underscore the intricate distribution of gas and dust contributing to the diverse array of AGN properties (e.g. Lyu & Rieke 2018; Esparza-Arredondo et al. 2021).

6. Conclusions

In this work, we used X-ray AGNs detected in the eFEDS and COSMOS-Legacy fields to study the SMBHs and host galaxy properties of type 1 and 2 AGNs. The sources were classified based on the results of the SED fitting analysis, using the CIGALE code. To ensure the robustness of our analysis, we applied stringent selection criteria, ensuring that only sources with reliable host galaxy properties and classifications were included. Consequently, our final dataset consists of 3312 sources, with approximately 85% of them located in the eFEDS field. Out of these sources, 3049 are type 1 AGNs and 263 are type 2 AGNs. We note, that according to previous studies, CIGALE’s classification performance has a success rate of about $\sim 80\text{--}85\%$. The primary findings of our study can be summarized as follows:

- Type 2 AGNs tend to inhabit more massive systems, by 0.2–0.3 dex (on a logarithmic scale), than their type 1 counterparts. Their specific black hole accretion rate, a proxy of the Eddington ratio, is on average lower in the case of type 2 sources compared to type 1, by ~ 0.3 dex on logarithmic scales.

These differences, although they only appear to have a statistical significance lower than 2σ , are observed across all redshifts and X-ray luminosities probed by our dataset ($0.5 < z < 3.5$, $42 < \log[L_{X,2-10\text{keV}}(\text{erg s}^{-1})] < 46$).

- Type 2 AGNs tend to have a lower SFR compared to type 1 AGNs at $z < 1$. Conversely, this picture reverses at high redshifts ($z > 2$) and X-ray luminosities ($\log[L_{X,2-10\text{keV}}(\text{erg s}^{-1})] > 44$). These differences are statistically significant at approximately a 2σ confidence level.
- Similar trends are discernible when we classify the 3312 AGNs based on their X-ray obscuration, applying a N_{H} cut at 10^{23} cm^{-2} . However, it is noteworthy that these observed differences are pronounced for non-luminous AGNs ($\log[L_{X,2-10\text{keV}}(\text{erg s}^{-1})] < 44$) and also tend to diminish when we lower the N_{H} threshold used for AGN classification.

The results from our analysis suggest that, irrespective of whether we employ optical or X-ray criteria to categorize AGNs as obscured or unobscured, the disparities in the host galaxy and SMBH properties between the two AGN populations exhibit similar trends. However, these differences are sensitive to the L_X regime probed and the stringency of the applied X-ray criteria. Thus, caution has to be taken when we compare results from different studies.

Acknowledgements. This project has received funding from the European Union's Horizon 2020 research and innovation program under grant agreement no. 101004168, the XMM2ATHENA project. This research has made use of TOPCAT version 4.8 (Taylor 2005) and Astropy (Astropy Collaboration 2022).

References

- Aird, J., Coil, A. L., & Georgakakis, A. 2018, *MNRAS*, 474, 1225
- Ananna, T. T., Urry, C. M., Ricci, C., et al. 2022, *ApJ*, 939, L13
- Arnouts, S., Cristiani, S., Moscardini, L., et al. 1999, *MNRAS*, 310, 540
- Astropy Collaboration (Price-Whelan, A. M., et al.) 2022, *ApJ*, 935, 167
- Baldry, I. K., Liske, J., Brown, M. J. I., et al. 2018, *MNRAS*, 474, 3875
- Blanton, M. R., Bershady, M. A., Abolfathi, B., et al. 2017, *AJ*, 154, 35
- Boquien, M., Burgarella, D., Roehlly, Y., et al. 2019, *A&A*, 622, A103
- Brunner, H., Liu, T., Lamer, G., et al. 2022, *A&A*, 661, A1
- Bruzual, G., & Charlot, S. 2003, *MNRAS*, 344, 1000
- Buat, V., Ciesla, L., Boquien, M., Małek, K., & Burgarella, D. 2019, *A&A*, 632, A79
- Buat, V., Mountrichas, G., Yang, G., et al. 2021, *A&A*, 654, A93
- Charlot, S., & Fall, S. M. 2000, *ApJ*, 539, 718
- Ciotti, L., & Ostriker, J. P. 1997, *ApJ*, 487, L105
- Civano, F., Marchesi, S., Comastri, A., et al. 2016, *ApJ*, 819, 62
- Dale, D. A., Helou, G., Magdis, G. E., et al. 2014, *ApJ*, 784, 83
- Drinkwater, M. J., Byrne, Z. J., Blake, C., et al. 2018, *MNRAS*, 474, 4151
- Elvis, M., Wilkes, B. J., McDowell, J. C., et al. 1994, *ApJS*, 95, 1
- Esparza-Arredondo, D., Gonzalez-Martín, O., Dultzin, D., et al. 2021, *A&A*, 651, A91
- Georgakakis, A., Aird, J., Schulze, A., et al. 2017, *MNRAS*, 471, 1976
- Georgantopoulos, I., Pouliaxis, E., Mountrichas, G., et al. 2023, *A&A*, 673, break A67
- Hernández-García, L., Masegosa, J., González-Martín, O., et al. 2017, *A&A*, 602, A65
- Hopkins, P. F., Hernquist, L., Cox, T. J., et al. 2006, *ApJS*, 163, 1
- Hopkins, P. F., Richards, G. T., & Hernquist, L. 2007, *ApJ*, 654, 731
- Ilbert, O., Arnouts, S., McCracken, H. J., et al. 2006, *A&A*, 457, 841
- Koutoulidis, L., Mountrichas, G., Georgantopoulos, I., Pouliaxis, E., & Plionis, M. 2022, *A&A*, 658, A35
- Kuijken, K., Heymans, C., Hildebrandt, H., et al. 2015, *MNRAS*, 454, 3500
- Kuijken, K., Heymans, C., Dvornik, A., et al. 2019, *A&A*, 625, A2
- Laigle, C., McCracken, H. J., Ilbert, O., et al. 2016, *ApJS*, 224, 24
- Lanzuisi, G., Delvecchio, I., Berta, S., et al. 2017, *A&A*, 602, A123
- Li, J., Xue, Y., Sun, M., et al. 2019, *ApJ*, 877, 5
- Liu, T., Buchner, J., Nandra, K., et al. 2022, *A&A*, 661, A5
- Lopez, I. E., Brusa, M., Bonoli, S., et al. 2023, *A&A*, 672, A137
- Lusso, E., Comastri, A., Simmons, B. D., et al. 2012, *MNRAS*, 425, 623
- Lyu, J., & Rieke, G. H. 2018, *ApJ*, 866, 92
- Małek, K., Buat, V., Roehlly, Y., et al. 2018, *A&A*, 620, A50
- Marchesi, S., Civano, F., Elvis, M., et al. 2016, *ApJ*, 817, 34
- Masoura, V. A., Mountrichas, G., Georgantopoulos, I., et al. 2018, *A&A*, 618, A31
- Masoura, V. A., Georgantopoulos, I., Mountrichas, G., et al. 2020, *A&A*, 638, A45
- Masoura, V. A., Mountrichas, G., Georgantopoulos, I., & Plionis, M. 2021, *A&A*, 646, A167
- McCracken, H. J., Milvang-Jensen, B., Dunlop, J., et al. 2012, *A&A*, 544, A156
- Menzel, M.-L., Merloni, A., Georgakakis, A., et al. 2016, *MNRAS*, 457, 110
- Merloni, A., Bongiorno, A., Brusa, M., et al. 2014, *MNRAS*, 437, 3550
- Mountrichas, G., & Buat, V. 2023, *A&A*, 679, A151
- Mountrichas, G., Georgakakis, A., & Georgantopoulos, I. 2019, *MNRAS*, 483, 1374
- Mountrichas, G., Georgantopoulos, I., Ruiz, A., & Kamyliis, G. 2020, *MNRAS*, 491, 1727
- Mountrichas, G., Buat, V., Georgantopoulos, I., et al. 2021a, *A&A*, 653, A70
- Mountrichas, G., Buat, V., Yang, G., et al. 2021b, *A&A*, 646, A29
- Mountrichas, G., Buat, V., Yang, G., et al. 2021c, *A&A*, 653, A74
- Mountrichas, G., Buat, V., Yang, G., et al. 2022a, *A&A*, 663, A130
- Mountrichas, G., Masoura, V. A., Xilouris, E. M., et al. 2022b, *A&A*, 661, A108
- Mountrichas, G., Viitanen, A., Carrera, F. J., et al. 2024, *A&A*, in press, <https://doi.org/10.1051/0004-6361/202348204>
- Neškova, M., Ivezić, Ž., & Elitzur, M. 2002, *ApJ*, 570, L9
- Netzer, H. 2015, *ARA&A*, 53, 365
- Ogawa, S., Ueda, Y., Tanimoto, A., & Yamada, S. 2021, *ApJ*, 906, 84
- Ordovas-Pascual, I., Mateos, S., Carrera, F. J., et al. 2017, *MNRAS*, 469, 693
- Park, T., Kashyap, V. L., Siemiginowska, A., et al. 2006, *ApJ*, 652, 610
- Pierre, M., Pacaud, F., Adami, C., et al. 2016, *A&A*, 592, A1
- Ricci, C., Trakhtenbrot, B., Koss, M. J., et al. 2017, *ApJS*, 233, 17
- Ruiz, A., Corral, A., Mountrichas, G., & Georgantopoulos, I. 2018, *A&A*, 618, A52
- Salvato, M., Hasinger, G., Ilbert, O., et al. 2009, *ApJ*, 690, 1250
- Salvato, M., Ilbert, O., Hasinger, G., et al. 2011, *ApJ*, 742, 61
- Salvato, M., Buchner, J., Budavári, T., et al. 2018, *MNRAS*, 473, 4937
- Salvato, M., Wolf, J., Dwelly, T., et al. 2022, *A&A*, 661, A3
- Scoville, N., Ausse, H., Brusa, M., et al. 2007, *ApJS*, 172, 1
- Shimizu, T. T., Davies, R. I., Koss, M., et al. 2018, *ApJ*, 856, 154
- Shirley, R., Roehlly, Y., Hurley, P. D., et al. 2019, *MNRAS*, 490, 634
- Shirley, R., Duncan, K., Varillas, M. C. C., et al. 2021, *MNRAS*, 507, 129
- Stalevski, M., Fritz, J., Baes, M., Nakos, T., & Popović, L. Č. 2012, *MNRAS*, 420, 2756
- Stalevski, M., Ricci, C., Ueda, Y., et al. 2016, *MNRAS*, 458, 2288
- Sutherland, W., & Saunders, W. 1992, *MNRAS*, 259, 413
- Taylor, M. B. 2005, in *Astronomical Data Analysis Software and Systems XIV*, eds. P. Shopbell, M. Britton, & R. Ebert, *ASP Conf. Ser.*, 347, 29
- Trippe, M. L., Crenshaw, D. M., Deo, R. P., et al. 2010, *ApJ*, 725, 1749
- Urry, C. M., & Padovani, P. 1995, *PASP*, 107, 803
- Villa-Velez, J. A., Buat, V., Theule, P., Boquien, M., & Burgarella, D. 2021, *A&A*, 654, A153
- Whittle, M. 1992, *ApJS*, 79, 49
- Wright, E. L., Eisenhardt, P. R. M., Mainzer, A. K., et al. 2010, *AJ*, 140, 1868
- Yang, G., Chen, C. T. J., Vito, F., et al. 2017, *ApJ*, 842, 72
- Yang, G., Boquien, M., Buat, V., et al. 2020, *MNRAS*, 491, 740
- Yang, G., Boquien, M., Brandt, W. N., et al. 2022, *ApJ*, 927, 192
- Zou, F., Yang, G., Brandt, W. N., & Xue, Y. 2019, *ApJ*, 878, 11